Dispersion-Engineered Metasurface Doublet Design for Broadband and Wide-Angle Operation in the Visible Range

Junhyeok Jang, Gun-Yeal Lee, Youngjin Kim, Changhyun Kim, Yoonchan Jeong, *Member, IEEE*, and Byoungho Lee, *Fellow, IEEE*

***Abstract*—The development of a metasurface lens, which represents a flat optical element with subwavelength thickness, holds the potential for miniaturizing imaging systems. Nevertheless, the presence of aberrations poses a significant challenge for achieving optimal imaging quality out of it. Moreover, its practical utilization in cameras and wearable devices necessitates simultaneous correction of monochromatic and chromatic aberrations. We here propose a framework to design multi-layered, dispersion-engineered metasurfaces, which is capable of correcting monochromatic and chromatic aberrations in a simultaneous manner. Based on the scheme, we numerically demonstrate a novel metasurface doublet that gives rise to significant improvement in correction of both monochromatic and chromatic aberrations. The designed lens has a field-of-view of 50° and operates in the broadband visible region from 450 to 650 nm.**

***Index Terms*—Aberration correction, flat optics, metalens, metasurface.**

I. Introduction

OPTICAL metasurfaces represent a novel class of planar diffractive optical elements consisting of high-density arrays of artificially engineered scatterers [1]. These scatterers can be finely tuned in terms of their size, shape, and spacing, to manipulate the properties of light selectively, including its amplitude, phase, and polarization. By exploiting these unique capabilities, metasurfaces have demonstrated the ability to replace traditional bulky optical components such as deflectors [2], [3], beam splitters [4], and holograms [5], [6], [7], [8]. Moreover, a system of metasurfaces integrated layer by layer has allowed for the precise control of the wavefront of light by varying its wavelength and incident angle. Recent demonstrations of miniaturized optical devices, such as spectrometers [9], [10], retroreflectors [11], and quantitative phase imaging [12], are good examples of them.

As one of the prominent applications of metasurfaces, metasurface lenses have been garnering a considerable amount of attention in that they have numerous advantages over traditional refractive lenses. Their form factor is entirely suitable for the use in compact optical systems including endoscope [13], augmented reality [14], and virtual reality devices [15], [16]. They can achieve high efficiency [17] and near-unity numerical aperture (NA) [18]. Additionally, the vast design freedom of the phase profile has even enabled the creation of a single-chip device for phase contrast imaging [19], [20], varifocal lenses [21] and depth sensing [22].

Despite such numerous benefits of metasurface lenses, there remains an issue that they are vulnerable to aberrations, which should, somehow, be corrected in order to achieve optimal imaging quality out of them [23]. Aberrations can be divided into two classes: chromatic and monochromatic. First, chromatic aberration is a well-established issue associated with the diffractive nature of metasurface lenses [24], which can limit the bandwidth of imaging systems. To address the chromatic aberration, researchers have employed various metasurface design schemes, such as the spatial multiplexing method [25], [26], the dispersion engineering [27], [28], [29], and the optimization [15], [16]. Second, monochromatic aberrations, most of which are associated with off-axis light, restrict the field-of-view (FOV) and result in low image quality. To achieve wide FOV, focusing performances have been relaxed by adopting symmetry transformation [30], [31], [32], while a computational approach has been utilized to restore the imaging quality [33]. Furthermore, alternative approaches involve the construction of doublet structures to fully realize the desired focusing capabilities [34], [35], [36].

In most metasurface lenses, chromatic and monochromatic aberrations have been addressed separately. For example, achromatic metasurface lenses inevitably exhibit considerable aberrations for high-angle incidence, and wide-FOV metasurface lenses are required to operate in a narrow bandwidth near the target wavelength, although some multi-layered metasurface lenses which could achieve a correction of both aberrations only at several discrete wavelengths have recently been demonstrated [37], [38]. In this light, compact and high-quality metasurface imaging systems still require simultaneous correction of

Manuscript received 3 May 2023; revised 5 June 2023; accepted 21 June 2023. Date of publication 26 June 2023; date of current version 10 July 2023. This work was supported by Samsung Science and Technology Foundation under Grant SRFC-IT2001-05. *(Corresponding author: Yoonchan Jeong.)*

Junhyeok Jang, Gun-Yeal Lee, Youngjin Kim, Changhyun Kim, and Yoonchan Jeong are with the Inter-University Semiconductor Research Center and Department of Electrical and Computer Engineering, Seoul National University, Seoul 08826, South Korea (e-mail: junh2119@snu.ac.kr; dlrjsduf12@snu.ac.kr; ttw8592@snu.ac.kr; kch3782@snu.ac.kr; yoonchan@snu.ac.kr).

Byoungho Lee, deceased, was with the Inter-University Semiconductor Research Center and Department of Electrical and Computer Engineering, Seoul National University, Seoul 08826, South Korea (e-mail: byoungho@snu.ac.kr).

Digital Object Identifier 10.1109/JPHOT.2023.3289588

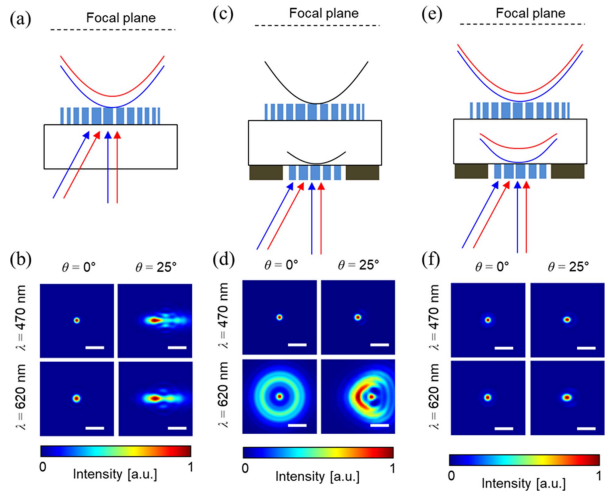

Fig. 1. Schematic illustration of metasurface lenses: (a) Single-layered, achromatic metasurface lens and (b) corresponding normalized intensity distributions by numerical simulation at the focal plane for wavelengths of 470 and 620 nm and incident angles of 0° and 25°. (c) Metasurface doublet designed for a wavelength of 470 nm and the FOV of 25° and (d) corresponding simulation results. (e) Dispersion-engineered metasurface doublet and (f) corresponding simulation results. Each metasurface lens has the same aperture diameter of 100 μm and NA of 0.1. The white bars in (b, d, and f) indicate 10 μm.

chromatic aberration in a broadband region and monochromatic aberration for the wide angle of incidence.

In this study, we present a novel approach for improving the performance of metasurface lenses by simultaneously correcting both monochromatic and chromatic aberrations. Our approach employs a doublet structure and dispersion engineering in the layers to extend the range of phase compensation, which enables overcoming the time-bandwidth limits of a single-layered structure. We design and numerically demonstrate a metasurface doublet operating in a broadband visible region of wavelengths ranging from 450 to 650 nm for incident angles up to 25°, including spherical, coma, and astigmatism. The designed metasurface doublet exhibits near diffraction-limited focusing performance in the broadband visible region, which is characterized by the point spread function (PSF) and the modulation transfer function (MTF). Our integrated scheme, including multi-layered system, dispersion engineering, and optimization, provides a promising foundation for improving metasurface lens performance, the details and evidences of which are to given in the sections that follow.

II. Design of Dispersion-Engineered Metasurface Doublet

The correction of chromatic aberration in a metasurface lens requires dispersive phase profiles (Fig. 1(a)). When designing a dispersion-engineered metasurface singlet with ideal hyperbolic phase profiles, the intensity profiles for normal incidence resemble an ideal airy disk (Fig. 1(b)). However, the profiles for oblique incidence at an angle of 25° tend to exhibit considerable monochromatic aberrations. On the other hand, a metasurface doublet with non-dispersive phase profiles can correct monochromatic aberrations for a single wavelength (Fig. 1(c)). When it operates for a wavelength of 470 nm, the simulation results show the distributions of aberration at a wavelength of 620 nm as presented in Fig. 1(d). These results suggest that the integration of the doublet structure and dispersion-engineered layers is necessary to achieve aberration-free imaging using metasurface lenses. To address this issue, we propose a cascade structure of dispersion-engineered metasurfaces for the simultaneous correction of chromatic and monochromatic aberrations (Fig. 1(e)). The simulation results of the proposed metasurface lens are presented in Fig. 1(f) for comparison.

To design the phase profiles of dispersion-engineered metasurface doublet, we use a gradient-based optimization approach as follows: First, we formulate a forward model to calculate the intensity profile at the focal plane for a system composed of a cascade of two metasurface layers. To calculate the gradient in the optimization process, we approximate the optical characteristics of meta-atoms as simple analytic functions. Second, we implement a scalar wave-optics simulation with a differentiable method and compute an objective function for focusing the incident light into a single spot. Third and finally, we compute its gradient and update the phase profiles to maximize the objective function.

A. Forward Model of Metasurface Doublet

A differentiable forward model for calculating the focal spots is formulated as follows: The complex amplitude of a planewave field with an angle θ tilted to x-axis and a wavelength λ is expressed as $E_{f-} = \exp[j(2\pi/\lambda)x\sin\theta]$. The transmitted field E_{f+} becomes the element-wise product $(\cdot)$ of E_{f-} and the transmittance $T_f = A_f \exp(j\varphi_f)$ of the frontside layer. We use the band-limited angular spectrum method (ASM) [39] as the wave propagation function $P_{\mathrm{ASM}}(E, \lambda, z, n)$ for the propagation of an incident field E of a wavelength λ by a distance z in the space of refractive index n. The wave propagating in the substrate of index n_{sub} by a substrate thickness z_1 and incident to the backside layer is expressed as $E_{b-} = P_{\mathrm{ASM}}(E_{f+}, \lambda, z_1, n_{\mathrm{sub}})$. Once again, the field transmitted from the backside layer of transmittance $T_b = A_b \exp(j\varphi_b)$ becomes $E_{b+} = E_{b-} \cdot T_{\mathrm{b}}$ and then propagates through the air. The output field at the focal plane, which is away from the backside layer by z_2, becomes $E_O = P_{\mathrm{ASM}}(E_{b+}, \lambda, z_2, n_{\mathrm{air}})$. The intensity profile $I_{\lambda,\theta}$ is calculated by the absolute square of E_O. All functions in this forward model, including the element-wise product, the ASM, the absolute square of complex number, are differentiable [40].

As each meta-atom exhibits inherent dispersion characteristics, the phase profiles φ_f and φ_b vary with frequency. To enable the metasurface lens to operate over a broad spectral range, it is crucial to ensure the continuity of the phase and group delay profiles. To achieve this, we introduce an optimizable profile $\rho(r)$, which represents the desired phase information for the designed meta-atoms in a radial coordinate r. We employ several approximation techniques to model the relationship between the optimizable value ρ and the phase delay ϕ of each meta-atom. In particular, we use a mapping approach that allows us to calculate the gradient of ϕ with respect to ρ. We describe the modeling processes for the frontside and backside of the proposed system

in Section II-B and II-C, respectively (see Appendix A for a flowchart of modelling the phase profiles).

Before modelling the phase profiles, it is necessary to determine with care the two configurations for designing multi-layered optical systems: polarization and the number of dispersion-engineered layers. The choice of polarization sensitivity affects the performance of the metasurface and has a significant impact on the design process. In our model, we assume that the incident light is left circularly polarized, and the output of the system is cross-polarized. The frontside layer is designed to be polarization-insensitive, as isotropic meta-atoms exhibit high diffraction efficiency over a broadband region (see Appendix B for simulation results on the diffraction efficiency). In the backside layer, anisotropic meta-atoms, which are polarization-sensitive, are designed to take advantage of Pancharatnam-Berry (PB) phase. Then, we control chromatic dispersions of both layers to extend the design freedom. We note that since chromatic dispersion occurs at every diffractive layer, excluding dispersion engineering in a certain layer would lead to deviation in focal length and focal shift between the wavelengths, causing chromatic aberration.

B. Design of Frontside Metasurface

Considering the previous research reports on demonstrating the achievement of titanium dioxide (TiO_2) doublet structures [35] and TiO_2 nano-pillars with higher aspect ratios [41], we employed an array of isotropic TiO_2 nano-pillars with square cross-sections and a thickness of 800 nm on the front side of the doublet, as shown in Fig. 2(a). The index of TiO_2 is quoted from experimental data [42]. The nano-pillars exhibit characteristics of truncated waveguides, and optical fields are concentrated inside, which is due to multiple Fabry-Perot resonances [43] (see Fig. 2(b)). As the refractive index of TiO_2 is sufficiently higher than the background index, near field couplings between the adjacent meta-atoms are hardly observed. As presented in Fig. 2(b), the coupled waveguide-modes in the nano-pillars vary with the wavelength of incident light. We investigate the dispersive nature of various meta-atoms to cover a wide range of group delays. The phases of the transmitted field with respect to width from 50 to 140 nm and wavelength from 450 to 700 nm are calculated (Fig. 2(c)). We carry out full-field electromagnetic simulations based on the rigorous coupled-wave analysis [44].

In the ideal truncated waveguide model, the relative phase delays of transmitted light can be expressed as $\phi(\omega) = (\omega/c)n_{\text{eff}}h$, where ω, c, n_{eff} and h denote the angular frequency, the speed of light, the effective index and the height of the nano-pillar, respectively. However, as the effective index is frequency-dependent, the phase delay ϕ may not be a linear function of frequency. To reduce the deviation of the approximately determined value from that obtained by the full numerical simulation, we represent the phase delay of the meta-atom in a given bandwidth around the target frequency ω_t in terms of the quadratic Taylor polynomial of frequency:

$$\phi(\omega) \simeq \phi(\omega_t) + \left.\frac{\partial\phi}{\partial\omega}\right|_{\omega=\omega_t}(\omega-\omega_t) + \frac{1}{2}\left.\frac{\partial^2\phi}{\partial\omega^2}\right|_{\omega=\omega_t}(\omega-\omega_t)^2. \quad (1)$$

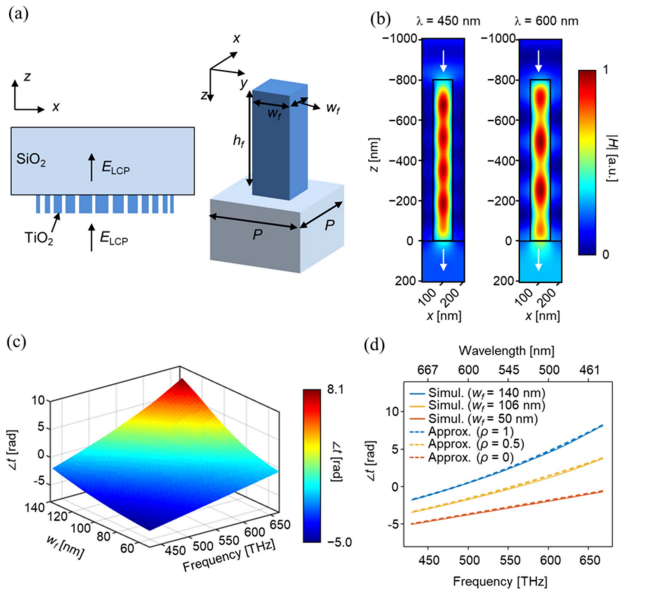

Fig. 2. Modelling meta-atoms on the frontside: (a) A schematic of the frontside metasurface composed of isotropic meta-atoms with square cross-sections, a period $P = 210$ nm, and a thickness $h_f = 800$ nm. The width w_f ranges from 50 to 140 nm. (b) Normalized magnetic field intensity $|H|$ distributions in xz-plane for normal incidence of wavelengths 450 and 600 nm ($w_f = 100$ nm). (c) Phase variations of transmission coefficients denoted by $\angle t$ with respect to width and frequency by numerical simulation. (d) Comparison between the phase delays (solid lines) for widths of 50, 106, and 140 nm by numerical simulation and the phase variations (dashed lines) for weights of 0, 0.5, and 1 by second-order approximation.

The full numerical simulation result presented in Fig. 2(c) confirms that the phase delay varies very monotonically without having any abrupt shifts in both width and wavelength axes. These results support that we can approximately represent the phase delay of an arbitrary meta-atom in the library using linear interpolation. We introduce a parameter ρ which contains the phase information of each meta-atom obtained by numerical simulation. This enables mapping of the single profile $\rho(r)$ to the phase profile $\varphi(r,\omega)$ at an arbitrary frequency within the given bandwidth. The phase delay of an arbitrary meta-atom with a width w_f can be expressed as follows:

$$\phi_{w_f}(\omega) = (1-\rho)\,\phi_{m,f}(\omega) + \rho\,\phi_{M,f}(\omega), \quad (2)$$

where the parameter ρ is a weight factor between 0 and 1 that is correlated with w_f; $\phi_{m,f}$ and $\phi_{M,f}$ denote the quadratic polynomials, which are fitted based on (1) and the simulation results, corresponding to each meta-atom with the minimum and maximum values of the group delay, respectively. In Fig. 2(d), the spectra obtained by the second-order approximation are compared with those obtained by numerical simulation when the values of ρ are given by 0, 0.5, and 1. In fact, they are in good agreement, so that it is reasonably acceptable to utilize the meta-atoms in the library for achieving optimized phase profiles with minimal deviations.

To construct a continuous phase and group delay profile, we introduce a radially symmetric weight profile $\rho_f(r) = \sum_{n=1}^{5} a_n (r/R_f)^{2n}$, where a_n, r and R_f denote the optimization coefficients, the radial coordinate, and the radius of the

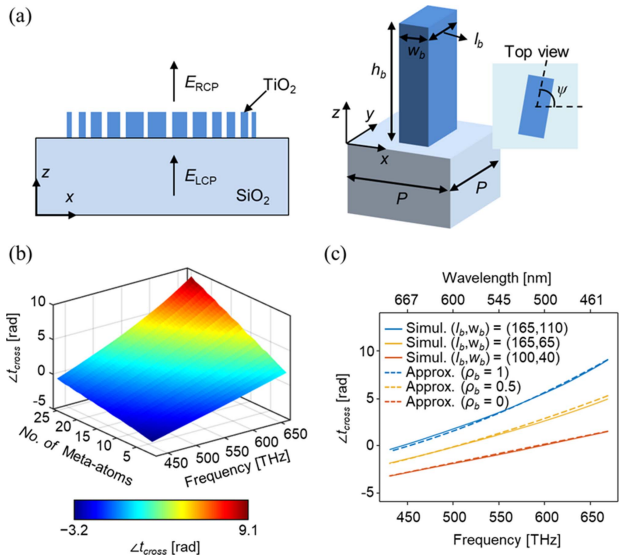

Fig. 3. Modelling of meta-atoms on the backside: (a) Schematic of the metasurface on the backside composed of anisotropic meta-atoms with rectangular cross-sections, a period of 210 nm, and a thickness of 800 nm. The length l_b ranges from 80 to 165 nm, and the width w_b ranges from 40 to 110 nm. (b) Phase variations of cross-polarized transmission coefficients denoted by $\angle t_{cross}$ for 25 meta-atoms in the order of ascending group delays by numerical simulation. (c) Comparison of the phase spectra (solid lines) for several meta-atoms of different geometric parameters (l_b, w_b) with the values determined by second-order approximation (dashed lines) for weight ρ of 0, 0.5, and 1.

metasurface on the frontside, respectively. Throughout this article, we employ even-order polynomials of *r* to ensure the radial symmetry of phase profiles. It is notable that this symmetry allows us to compute the forward model of oblique incidences along a single axis for characterizing the entire FOV, which helps enhance the computational efficiency in the optimization process. We constrain the values of the weight profile $\rho_f(r)$ to a range between 0 and 1 using the min-max feature scaling method, i.e., $\rho' = [\rho - \min(\rho)] / [\max(\rho) - \min(\rho)]$, for each corresponding meta-atom in the library. Finally, by replacing ρ in (2) with ${\rho'}_f(r)$, we obtain the phase profile of the metasurface on the frontside as follows:

$$\varphi_f(r,\omega) = \left(1 - {\rho'}_f(r)\right)\phi_m + {\rho'}_f(r)\,\phi_M. \tag{3}$$

C. Design of Backside Metasurface

For the backside, we use anisotropic TiO_2 nano-pillars with rectangular cross-sections to achieve the PB phase as shown in Fig. 3(a). These anisotropic nano-pillars can convert incident circularly polarized light into its orthogonal counterpart, owing to the difference in complex transmission coefficients polarized along the long and short axes. Using the Jones calculus [43], the transmission coefficient of the cross-polarized light is derived as follows:

$$t_{cross} = \frac{(t_l - t_s)}{2}\exp(j2\psi), \tag{4}$$

where *l* and *s* denote the long and short axes of the nano-pillars, respectively, and ψ denotes the orientation angle of the nano-pillar. It can be seen from (4) that the rotation of nano-pillars can induce a uniform phase shift of 2ψ, irrespective of wavelength.

We also investigate the chromatic dispersion of various meta-atoms on the backside to fulfill the group delay requirement. The period and thickness of the backside are kept the same as those of the frontside. We calculate the cross-polarized transmission coefficients of various geometric parameters with a length range from 80 to 165 nm and a width range from 40 to 110 nm by numerical simulation. We employ 25 meta-atoms exhibiting different chromatic dispersion as shown in Fig. 3(b). As they exhibit monotonic dispersion characteristics similar to the frontside, the phase delays can be approximately determined using the same method as the frontside (Fig. 3(c)). We can obtain the weight profile ${\rho_b}'(r)$ having a range of 0 to 1 from scaling the even-order polynomial $\rho_b(r) = \sum_{n=1}^{5} b_n (r/R_b)^{2n}$, where b_n and R_b denote the optimization coefficients and the radius of the backside layer, respectively. We can define a phase profile exhibiting the dispersion of anisotropic meta-atoms as follows:

$$\varphi_{ani}(r,\omega) = \left(1 - {\rho'}_b(r)\right)\phi_{m,b} + {\rho'}_b(r)\,\phi_{M,b}, \tag{5}$$

where $\phi_{m,b}$ and $\phi_{M,b}$ denote the quadratic polynomials, which are fitted based on (1) and the simulation results, corresponding to each meta-atom with the minimum and maximum values of the group delay, respectively. We can define the phase profile of the backside layer as follows:

$$\varphi_b(r,\omega) = \varphi_{ani}(r,\omega) + \varphi_{PB}(r), \tag{6}$$

with the introduction of the PB phase term $\varphi_{PB}(r) = \sum_{n=1}^{5} c_n (r/R_b)^{2n}$, where c_n's denote the optimization coefficients. This additional phase term, achieved by the rotation of the meta-atoms, eventually enables us to find the target phase profile required in the broadband region.

D. Gradient-Based Optimization

We formulate a differentiable forward model and define two dispersive phase profiles, $\varphi_f(r,\omega)$ and $\varphi_b(r,\omega)$, to design a metasurface lens using the gradient-based optimization (see Appendix C for the detailed optimization pipeline). We assume that both metasurface layers have ideal phase profiles with amplitudes of unity. The optimization process starts with random values for optimization coefficients of a_n, b_n, and c_n. We obtain the intensity profiles at the target focal plane by repeatedly applying incident plane waves with three angles $\theta = 0°$, 12.5°, and 25° and seven wavelengths λ = 450, 474, 501, 532, 566, 605, and 650 nm. Note that these wavelengths are selected such that they result in the same frequency interval between any two adjacent wavelengths in the wavelength range of 450 to 650 nm. We set the objective function as a weighted sum of the maximum intensity values at the target focal plane as follows:

$$O = \sum_{\lambda}\sum_{\theta} \eta_{\lambda,\theta} \max_{\mathbf{x}} \left[\left|I_{\lambda,\theta}(\mathbf{x})\right|^2\right], \tag{7}$$

where $\mathbf{x}$ is a spatial position at the focal plane and $\eta_{\lambda,\theta}$ is weights for rescaling the maximum intensity across different wavelengths and incident angles. Our forward model for obtaining the objective function is fully differentiable, so that we can efficiently compute the gradients using backpropagation and update the optimization coefficients via the Adam optimizer

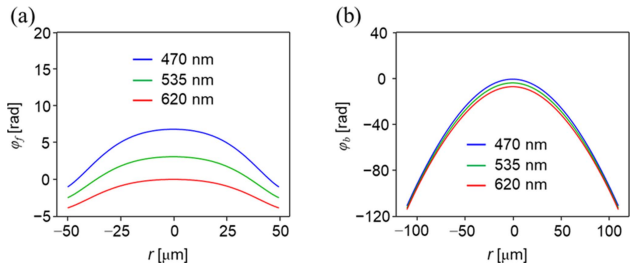

Fig. 4. Optimization results of the metasurface doublet: Optimized phase profiles at different wavelengths on (a) the frontside and (b) the backside.

TABLE I
OPTIMIZED COEFFICIENTS OF THE METASURFACE DOUBLET

a_1	a_2	a_3	a_4	a_5
−241.48	−324.68	218.13	10.16	0.56
b_1	b_2	b_3	b_4	b_5
−123.42	−850.18	674.52	−11.47	−6.92
c_1	c_2	c_3	c_4	c_5
−121.30	13.56	−1.86	−0.52	−0.07

[45]. We implement this optimization process iteratively 5000 times until the objective function converges.

III. RESULTS

Fig. 4 shows the optimized phase profiles of the metasurface doublet at three wavelengths (470, 535, and 620 nm). All the optimization coefficients used in the Section III are summarized in Table I. The coefficients a_n are polynomial coefficients related to the dispersion of meta-atoms in the frontside layer, and the coefficients b_n and c_n are polynomial coefficients related to the dispersion of meta-atoms and PB phase in the backside layer, respectively. The frontside of the designed lens has an aperture diameter of 100 μm, while the backside has a diameter of approximately 214 μm to prevent vignetting for oblique incidence up to 25°. The designed lens has an NA of 0.1, corresponding to an effective focal length of approximately 498 μm. The distances between two metasurface layers and between the backside layer and the target back focal plane are 200 μm and 453.3 μm, respectively. The deviation between the back focal plane and the effective focal length results from the contribution of the frontside layer to converging the light. The frontside layer with a narrow diameter acts as a dispersion-engineered corrector, while the backside layer has similar profiles to those of a dispersion-engineered lens and predominantly contributes to focusing the light.

We analyze the performance of the designed metasurface doublet by calculating the intensity distributions at the focal plane for five wavelengths of 470, 500, 535, 574, and 620 nm and three incident angles of 0°, 12.5°, and 25°. These wavelengths are selected such that they result in the same frequency interval between any two adjacent wavelengths in the wavelength rage of 470 to 620 nm. We replace the optimized profiles in Fig. 4 with the complex transmission coefficients simulated and finely adjust φ_{PB} to minimize the phase error. As shown in Fig. 5(a),

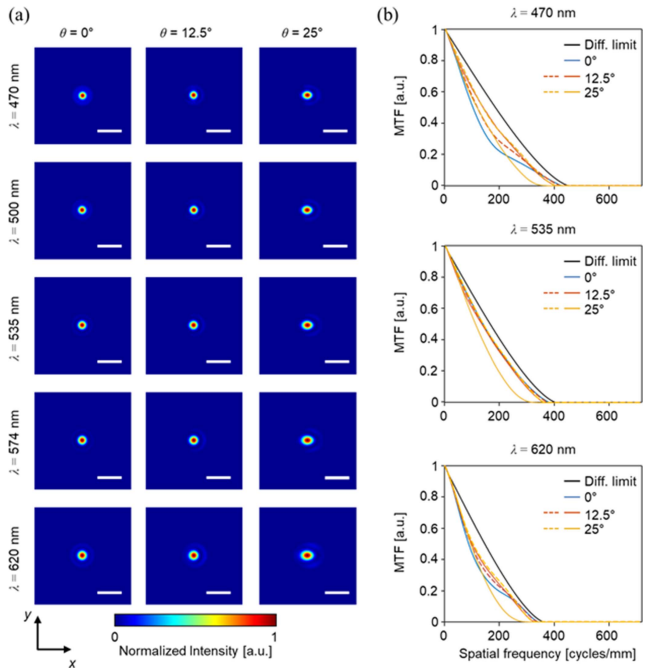

Fig. 5. Simulation results for the focal spots and modulation transfer functions (MTF) of the designed lens: (a) Normalized intensity distributions (xy-plane) at the focal spot for oblique incident angles of 0°, 12.5°, and 25° with respect to x-axis and wavelengths of 470, 500, 535, 574, and 620 nm. The length of the white bars indicates 10 μm. (b) MTF for wavelengths of 470, 535, and 620 nm. The solid and dashed lines are the MTF for tangential planes and sagittal planes, respectively. The black lines indicate the MTF of the diffraction-limited system with the same aperture diameter of 100 μm and NA of 0.10.

sidelobes near the focal spots are significantly suppressed, compared with other metasurface lenses in Fig. 1. For the incident angle of 0° and 12.5°, the intensity distributions are close to ideal airy disks, as indicated by the MTFs in Fig. 5(b). The MTFs, which represent how well an optical system reproduces the fine details of an object in the image, are as good as to those of diffraction-limited systems with the same aperture diameter and NA. The MTFs are obtained by taking the modulus of the Fourier transform of the intensity distributions in Fig. 5(a) [39]. For an incident angle of 25°, the focal spots also show improved distributions compared to Fig. 1; however, slight differences between the tangential plane (x-axis) and sagittal plane (y-axis) are observed. The astigmatism for high incident angles is not exhibited in the optimization results with ideal phase profiles, indicating that it arises from the phase deviations between the optimized and realized profiles. This deviation can be further suppressed by using an interpolation method to predict the characteristics of random meta-atoms [16]. In addition, our doublet also exhibits improved focusing characteristics for other wavelengths and angles within the bandwidth and the full FOV (see Appendix D for simulation results).

We evaluate the imaging performance of the designed lens in terms of monochromatic and chromatic aberrations compared to a conventional metasurface lens. We obtain the output images produced by the metasurface lenses by convolving the target images with corresponding PSFs. We employ the overlap-add method for the space-variant system [46]. This method involves cutting the target image into overlapping sections and damping

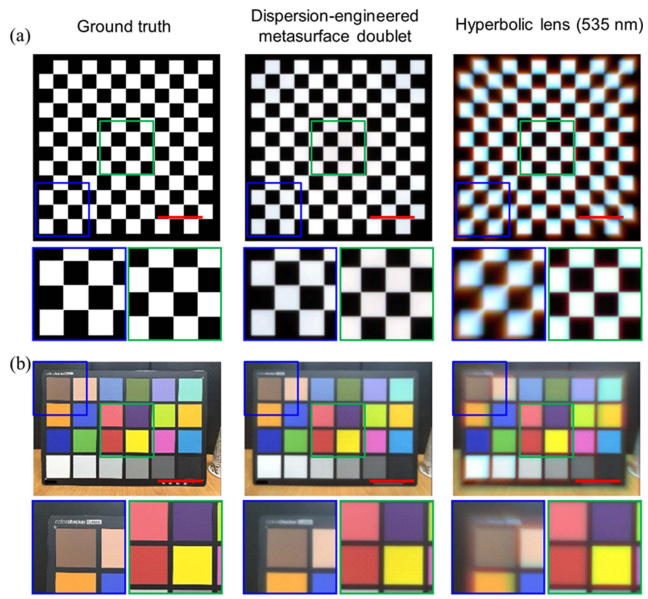

Fig. 6. Image formation of metasurface lenses: (a) A binary image of the checker pattern and (b) a captured image of the color checkerboard numerically reconstructed. Compared with a hyperbolic lens designed for a single wavelength of 535 nm, the dispersion-engineered metasurface doublet reconstructs aberration-corrected images with the high quality. The length of the red bars indicates 100 μm.

TABLE II
QUANTITATIVE COMPARISON OF IMAGE QUALITY BETWEEN METASURFACE LENS DESIGN METHODS

Image	Method	Red		Green		Blue		Full-color	
		MSE	PSNR	MSE	PSNR	MSE	PSNR	MSE	PSNR
Binary image	Hyperbolic	0.1184	9.27	0.0441	13.55	0.0282	15.49	0.0636	11.97
	Our work	0.0236	16.26	0.0191	17.19	0.0179	17.48	0.0202	16.95
Captured image	Hyperbolic	0.0408	13.90	0.0115	19.40	0.0065	21.88	0.0196	17.08
	Our work	0.0080	20.00	0.0053	22.73	0.0045	23.48	0.0059	22.27

the overlapping sections with a windowing function. Each section is then convolved with the same PSF, and the output image is generated by adding the transformed sections. Fig. 6 shows the results of image formation for a binary image of the checker pattern and a captured image of the color checkerboard. The images are resized, considering the FOV and the aperture size of metasurface lenses. A hyperbolic metasurface lens optimized for a wavelength of 535 nm reconstructs low-quality images that exhibit chromatic aberration near the center and both chromatic and monochromatic aberrations at the corner. On the other hand, the proposed lens reconstructs the images with higher quality in aberration corrections. These improvements can also be quantitatively validated using the mean-squared error (MSE) and the peak signal-to-noise ratio (PSNR), as shown in Table II.

Fig. 7 presents various performance indicators of the designed lens. The Strehl ratio (SR), which indicates the overall imaging quality [39], [47], is calculated from the MTFs in Fig. 5(b) and plotted in Fig. 7(a). A hyperbolic metasurface lens designed for a wavelength of 535 nm is used as a comparison device. In the case of the hyperbolic lens, the SRs at wavelengths of 470 and 620 nm are low due to chromatic aberration and decreases significantly with incident angle even at the target wavelength. In contrast, the degradation of the SR with incident angle is remarkably

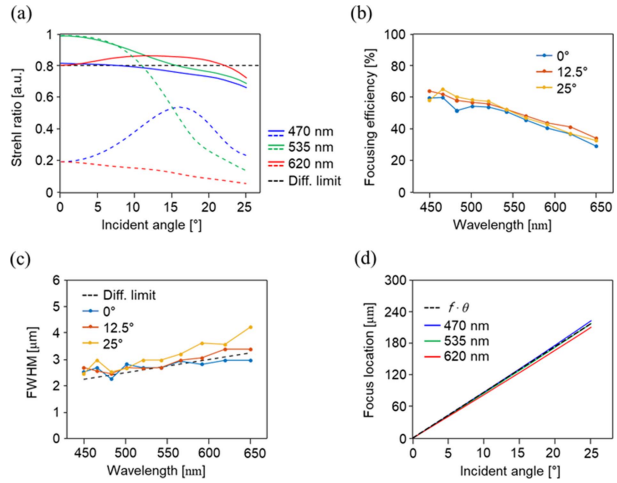

Fig. 7. Focusing performance indicators of the designed metasurface doublet: (a) Strehl ratios (SRs) as a function of incident angle for different wavelengths of 470, 535, and 620 nm. The solid and dashed lines in (a) are the SRs of the designed lens and a hyperbolic metasurface lens. The black dashed line in (a) is a lower boundary of the diffraction-limited system. (b) Focusing efficiency and (c) full width at half maximum (FWHM) as a function of wavelength for different incident angles of 0°, 12.5° and 25°. The black dashed line in (c) corresponds to the ideal value of λ / 2NA. (d) Transverse shift of the focus location as a function of incident angle for different wavelengths of 470, 535, and 620 nm. The black dashed line in (d) plots a product of the focal length and incident angles.

improved in our doublet. The SR for normal incidence is higher than the lower limit of 0.8 for the diffraction-limited system within the wavelength range of 470 to 620 nm. Our doublet shows SRs exceeding 0.6 across the wavelengths from 450 to 650 nm and for incident angles up to 25°. These results indicate that the wavefront error of our doublet remains below 10% [48], underscoring the high performance of our doublet design under a broad-range condition (see Appendix D for detailed SRs). Focusing efficiencies, defined as the ratio of the focused power within the observed focal spot of Fig. 5(a) to the power incident to the aperture, are predominantly influenced by the diffraction efficiency of the meta-atoms (Fig. 7(b)). While the diffraction efficiencies of meta-atoms on the frontside are near unity in the given bandwidth, polarization conversion efficiencies of meta-atoms on the backside show fluctuations (see Appendix B for detailed diffraction efficiencies). These fluctuations can be alleviated by further investigating the complex geometry for high efficiency in the broadband region using topology optimization [49]. Full width at half maximum (FWHM) values obtained from Fig. 5(a) are close to the ideal values λ/2NA for the diffraction-limited system (Fig. 7(c)), ensuring good focusing performance within the given bandwidth and angles. The transverse shift, which is defined as the position of the maximum intensity at the target focal plane according to the angle of incidence, is calculated in Fig. 7(d). The shifts are linear with the angle of incidence along a plot of $f{\cdot}\theta$. The linearity corresponds to that of a fisheye lens with the equidistant projection [50]. However, judging from deviations between the wavelengths, transverse chromatic aberration is not perfectly corrected.

Our proposed design methodology is versatile, being capable of accommodating varying spectra and higher angles through

simple modifications to several design parameters. By investigating different meta-atoms, metasurface doublets capable of operating in a distinct spectral range can be systematically designed. An increased FOV, which is frequently required in devices such as cameras and near-eye displays, can be realized by augmenting the diameter of the backside element, thus preventing vignetting. It should be noted, however, that any increase in diameter, including that on the frontside, necessitates a broader range of group delays in our design scheme, which is a typical characteristic of most achromatic metasurface lenses. By employing advanced fabrication techniques, for instance, fabricating TiO_2 nano-pillars with greater aspect ratios [41], a larger group delay range can be feasibly achieved. Furthermore, prospective advancements in fabrication technology, such as nano-hole structures with higher aspect ratios [51] and a technique for spatially modulating the height [52], may present additional opportunities for enhancing the performance of achromatic lenses.

IV. Conclusion

We have demonstrated a broadband achromatic metasurface doublet for wide-angle imaging in the visible range through a novel design method. Specifically, we have presented a framework of metasurface lens design, including a doublet structure, dispersion engineering, and gradient-based optimization, for simultaneously correcting chromatic and monochromatic aberrations. The designed metasurface doublet, with an aperture diameter of 100 μm and NA of 0.1, achieved close-to-diffraction-limited focusing performance from 470 to 620 nm and considerably improved correction of monochromatic aberrations within an incident angle of 25°. While transverse chromatic aberration was not completely corrected, it could be mitigated by post-processing in imaging systems equipped with sensors and computing power, such as digital cameras and mobile devices. We believe that our strategy for designing aberration-corrected, multi-layered metasurface lenses can be a stepping stone for miniaturized imaging systems used in various applications, such as virtual reality, augmented reality, and bio-imaging.

Appendix A
Modelling Phase Profiles

In Section II-B and II-C, we have proposed a differentiable metasurface model approximating the optical response of the meta-atoms. This enables to optimize the metasurface doublet based on the ASM which is a memory-efficient method. A flowchart for approximation of the metasurface is shown in Fig. 8. We calculate the transmission coefficients of meta-atoms using the RCWA [44]. Based on the simulation results, we fit the phase spectra of two meta-atoms with the lowest and highest group delay by quadratic Taylor polynomials ϕ_m and ϕ_M, respectively. We approximate a phase spectrum ϕ_i of an arbitrary meta-atom in the library by linear interpolation of two fitted spectra. The validity of the approximation can be ensured by comparison of fitted phase spectra and simulated results. The value of a weight ρ for interpolation reflects the phase information of the distinct meta-atom. Therefore, by introducing

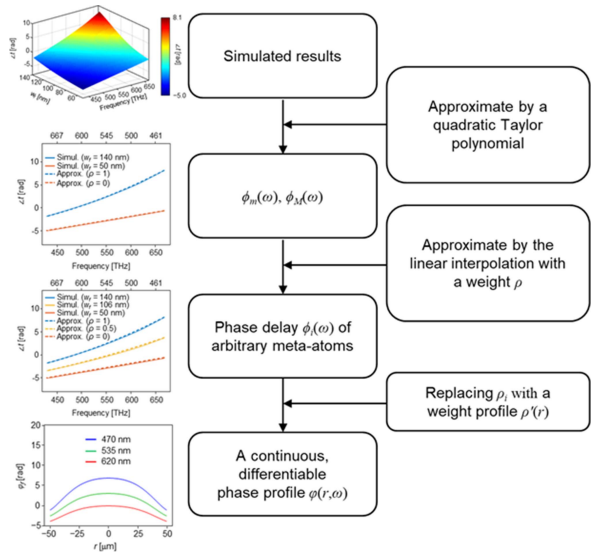

Fig. 8. Flowchart for modelling dispersive phase profiles which are supposed to be continuous and differentiable. Based on the simulation results, phase delays of two meta-atoms exhibiting the lowest and the highest group delay are approximated by quadratic Taylor polynomials (ϕ_m, ϕ_M). By using the linear interpolation of two polynomials with a weight ρ, the phase delay ϕ_i of arbitrary meta-atoms in the library can be approximated. A continuous and differentiable weight profile $\rho'(r)$ in a radial coordinate r is introduced to characterize the spatial distribution of meta-atoms. By replacing a scalar weight ρ with a scaled weight profile $\rho'(r)$, we can define a continuous and differentiable phase profile that reflects the chromatic dispersion of meta-atoms.

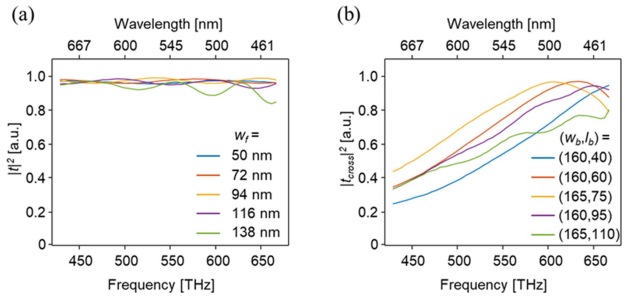

Fig. 9. Transmission spectra of meta-atoms numerically simulated for each layer of the metasurface doublet: (a) Transmission coefficients of meta-atoms on the frontside with $w_f = 50$, 72, 94, 116, and 138 nm. (b) Cross-polarized transmission coefficients of meta-atoms on the backside with geometric parameters $(l_b, w_b) = (160, 40)$, (160, 60), (165, 75), (160, 95), and (165, 110).

continuous and differentiable scaled profile $\rho'(r)$ in a radial coordinate r, we can define a continuous and differentiable phase profile.

Appendix B
Transmission of Meta-Atoms

To design the metasurface doublet, we utilize 45 isotropic meta-atoms for the frontside layer and 25 anisotropic meta-atoms for the backside layer. Fig. 9 shows simulated transmission spectra of several meta-atoms used in each layer. The intensities of meta-atoms in the frontside layer are high within the given bandwidth. The conversion spectra of the meta-atoms in the backside layer are varied with wavelengths, which affects the focusing efficiency shown in Fig. 7(b).

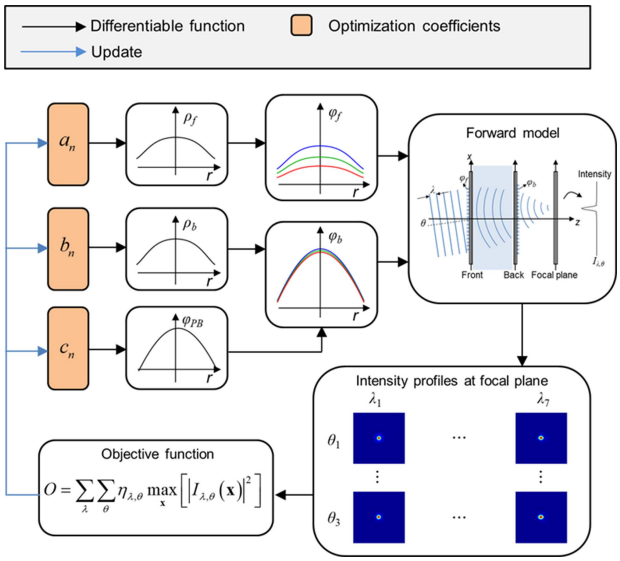

Fig. 10. Optimization flowchart: From the optimization coefficients, our differentiable model produces intensity profiles at the focal plane under different conditions of wavelengths and incident angles. Using the gradients of the objective function, the optimization coefficients are updated.

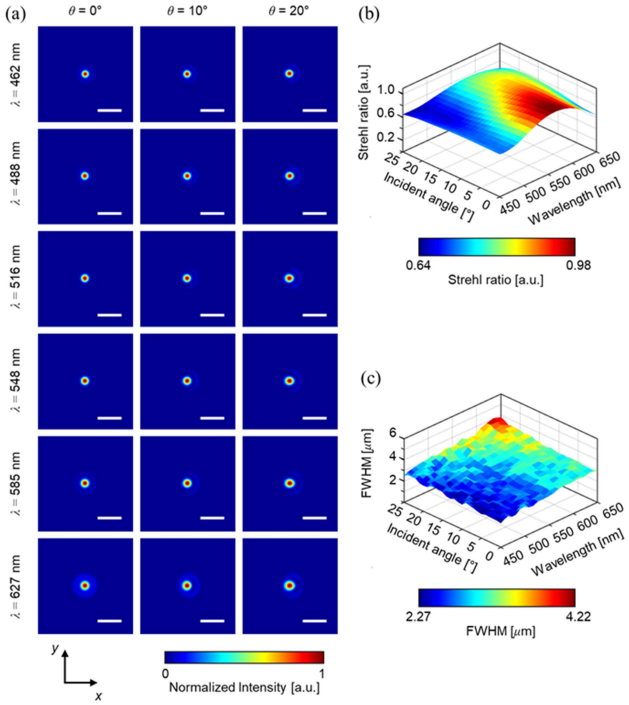

Fig. 11. Broadband and wide-angle characteristics of the proposed metasurface doublet: (a) Normalized intensity distributions (*xy*-plane) at the focal spot for oblique incident angles of 0°, 10°, and 20° with respect to *x*-axis and wavelengths of 462, 488, 516, 548, 585, and 627 nm. The length of the white bars indicates 10 μm. (b) SRs and (c) FWHMs are calculated across the wavelength region of 450 to 650 nm and the incident angle of 0° to 25°.

Appendix C
Optimization Pipeline

Our approach to the design of the metasurface doublet is realized through the optimization process depicted in Fig. 10. This involves deriving the weight profiles ρ_f and ρ_b as radial polynomials from the optimization coefficients a_n and b_n. Concurrently, the optimization coefficient c_n is used to define a uniform phase profile φ_{PB} within the broadband region as a radial polynomial. Subsequently, we derive the frontside phase profiles φ_f from ρ_f using appropriate approximations. Similarly, the backside phase profiles φ_b are obtained through integration of φ_{ani} and φ_{PB}, with φ_{ani} being derived from ρ_b via suitable approximations. Utilizing φ_f and φ_b, we formulate the forward model that calculates the intensity profile at the focal plane. The intensity profiles are calculated at different wavelengths and incident angles. Finally, the objective function is derived as a weighted sum of the maximum intensities. Crucially, the pipeline for the computation of the objective function entirely consists of differentiable functions. The inherent differentiability of this pipeline facilitates joint optimization of the coefficients. The gradients of the objective function are computed using the backpropagation, and then the coefficients are updated.

Appendix D
Broadband Achromatic and Wide-Angle Characterization

To validate the broadband and wide-angle operation of the metasurface doublet proposed, we additionally characterize the focal spots under diverse conditions that have not been used for optimization. Fig. 11(a) shows the intensity distributions at the focal plane at wavelengths of 462, 488, 516, 548, 585, and 627 nm and for incident angles of 0°, 10°, and 20°. In order for further supporting the performance of the doublet, we also present the SRs and the FWHMs across the wavelength range from 450 to 650 nm, and for the incident angles ranging from 0° to 25° in Fig. 11(b) and (c). Notably, the SRs are higher than 0.64, and the FWHMs are evenly distributed with minimal fluctuations under the given simulation conditions. The close approximation of the FWHMs in Fig. 7(c) to the ideal values implies that the overall FWHMs in Fig. 11(c) also meet the desired standards. These results affirm the effective suppression of aberrations and the focusing performances within the broadband region, as well as across the entire FOV.

Acknowledgment

We would like to acknowledge the contributions of B. L., who unfortunately passed away during the course of this research. We are deeply grateful for his contributions, and he will be greatly missed.

References

[1] N. Yu and F. Capasso, "Flat optics with designer metasurfaces," *Nature Mater.*, vol. 13, no. 2, pp. 139–150, Jan. 2014, doi: 10.1038/nmat3839.
[2] C. Choi, T. Choi, J.-G. Yun, C. Yoo, and B. Lee, "Two-dimensional angular bandwidth broadening of metasurface grating," *Adv. Photon. Res.*, vol. 3, no. 12, Aug. 2022, Art. no. 2200158, doi: 10.1002/adpr.202200158.
[3] D. Lin, P. Fan, E. Hasman, and M. L. Brongersma, "Dielectric gradient metasurface optical elements," *Science*, vol. 345, no. 6194, pp. 298–302, Jul. 2014, doi: 10.1126/science.1253213.
[4] B. Wang et al., "Rochon-prism-like planar circularly polarized beam splitters based on dielectric metasurfaces," *Amer. Chem. Soc. Photon.*, vol. 5, no. 5, pp. 1660–1664, Dec. 2017, doi: 10.1021/acsphotonics.7b01191.

[5] J. Sung, G. Y. Lee, C. Choi, J. Hong, and B. Lee, "Single-layer bifacial metasurface: Full-space visible light control," *Adv. Opt. Mater.*, vol. 7, no. 8, Feb. 2019, Art. no. 1801748, doi: 10.1002/adom.201801748.

[6] J. Jang, G. Y. Lee, J. Sung, and B. Lee, "Independent multichannel wavefront modulation for angle multiplexed meta-holograms," *Adv. Opt. Mater.*, vol. 9, no. 17, Sep. 2021, Art. no. 2100678, doi: 10.1002/adom.202100678.

[7] G.-Y. Lee, J. Sung, and B. Lee, "Metasurface optics for imaging applications," *J. Mater. Res. Bull.*, vol. 45, no. 3, pp. 202–209, Sep. 2020, doi: 10.1557/mrs.2020.64.

[8] G. Y. Lee et al., "Complete amplitude and phase control of light using broadband holographic metasurfaces," *Nanoscale*, vol. 10, no. 9, pp. 4237–4245, Mar. 2018, doi: 10.1039/c7nr07154j.

[9] M. Faraji-Dana, E. Arbabi, A. Arbabi, S. M. Kamali, H. Kwon, and A. Faraon, "Compact folded metasurface spectrometer," *Nature Commun.*, vol. 9, no. 1, Oct. 2018, Art. no. 4196, doi: 10.1038/s41467-018-06495-5.

[10] A. Y. Zhu et al., "Compact aberration-corrected spectrometers in the visible using dispersion-tailored metasurfaces," *Adv. Opt. Mater.*, vol. 7, no. 14, Dec. 2018, Art. no. 1801144, doi: 10.1002/adom.201801144.

[11] A. Arbabi, E. Arbabi, Y. Horie, S. M. Kamali, and A. Faraon, "Planar metasurface retroreflector," *Nature Photon.*, vol. 11, no. 7, pp. 415–420, Jun. 2017, doi: 10.1038/nphoton.2017.96.

[12] H. Kwon, E. Arbabi, S. M. Kamali, M. Faraji-Dana, and A. Faraon, "Single-shot quantitative phase gradient microscopy using a system of multifunctional metasurfaces," *Nature Photon.*, vol. 14, no. 2, pp. 109–114, Oct. 2019, doi: 10.1038/s41566-019-0536-x.

[13] H. Pahlevaninezhad et al., "Nano-optic endoscope for high-resolution optical coherence tomography in vivo," *Nature Photon.*, vol. 12, no. 9, pp. 540–547, Sep. 2018, doi: 10.1038/s41566-018-0224-2.

[14] G. Y. Lee et al., "Metasurface eyepiece for augmented reality," *Nature Commun.*, vol. 9, no. 1, Nov. 2018, Art. no. 4562, doi: 10.1038/s41467-018-07011-5.

[15] Z. Li et al., "Meta-optics achieves RGB-achromatic focusing for virtual reality," *Sci. Adv.*, vol. 7, no. 5, Jan. 2021, Art. no. eabe4458, doi: 10.1126/sciadv.abe4458.

[16] Z. Li, R. Pestourie, J. S. Park, Y. W. Huang, S. G. Johnson, and F. Capasso, "Inverse design enables large-scale high-performance meta-optics reshaping virtual reality," *Nature Commun.*, vol. 13, no. 1, May 2022, Art. no. 2409, doi: 10.1038/s41467-022-29973-3.

[17] R. C. Devlin, M. Khorasaninejad, W. T. Chen, J. Oh, and F. Capasso, "Broadband high-efficiency dielectric metasurfaces for the visible spectrum," *Proc. Nat. Acad. Sci.*, vol. 113, no. 38, pp. 10473–10478, Sep. 2016, doi: 10.1073/pnas.1611740113.

[18] R. Paniagua-Dominguez et al., "A metalens with a near-unity numerical aperture," *Nano Lett.*, vol. 18, no. 3, pp. 2124–2132, Mar. 2018, doi: 10.1021/acs.nanolett.8b00368.

[19] P. Huo et al., "Photonic spin-multiplexing metasurface for switchable spiral phase contrast imaging," *Nano Lett.*, vol. 20, no. 4, pp. 2791–2798, Apr. 2020, doi: 10.1021/acs.nanolett.0c00471.

[20] Y. Kim, G. Y. Lee, J. Sung, J. Jang, and B. Lee, "Spiral metalens for phase contrast imaging," *Adv. Funct. Mater.*, vol. 32, no. 5, Jan. 2022, Art. no. 2106050, doi: 10.1002/adfm.202106050.

[21] M. D. Aiello et al., "Achromatic varifocal metalens for the visible spectrum," *Amer. Chem. Soc. Photon.*, vol. 6, no. 10, pp. 2432–2440, Sep. 2019, doi: 10.1021/acsphotonics.9b00523.

[22] Q. Guo et al., "Compact single-shot metalens depth sensors inspired by eyes of jumping spiders," *Proc. Nat. Acad. Sci.*, vol. 116, no. 46, pp. 22959–22965, Nov. 2019, doi: 10.1073/pnas.1912154116.

[23] W. T. Chen, A. Y. Zhu, and F. Capasso, "Flat optics with dispersion-engineered metasurfaces," *Nature Rev. Mater.*, vol. 5, no. 8, pp. 604–620, Aug. 2020, doi: 10.1038/s41578-020-0203-3.

[24] F. Presutti and F. Monticone, "Focusing on bandwidth: Achromatic metalens limits," *Optica*, vol. 7, no. 6, pp. 624–631, Jun. 2020, doi: 10.1364/optica.389404.

[25] D. Lin et al., "Photonic multitasking interleaved Si nanoantenna phased array," *Nano Lett.*, vol. 16, no. 12, pp. 7671–7676, Dec. 2016, doi: 10.1021/acs.nanolett.6b03505.

[26] E. Arbabi, A. Arbabi, S. M. Kamali, Y. Horie, and A. Faraon, "Multiwavelength polarization-insensitive lenses based on dielectric metasurfaces with meta-molecules," *Optica*, vol. 3, no. 6, pp. 628–633, Jun. 2016, doi: 10.1364/optica.3.000628.

[27] W. T. Chen et al., "A broadband achromatic metalens for focusing and imaging in the visible," *Nature Nanotechnol.*, vol. 13, no. 3, pp. 220–226, Mar. 2018, doi: 10.1038/s41565-017-0034-6.

[28] S. Wang et al., "A broadband achromatic metalens in the visible," *Nature Nanotechnol.*, vol. 13, no. 3, pp. 227–232, Mar. 2018, doi: 10.1038/s41565-017-0052-4.

[29] W. T. Chen, A. Y. Zhu, J. Sisler, Z. Bharwani, and F. Capasso, "A broadband achromatic polarization-insensitive metalens consisting of anisotropic nanostructures," *Nature Commun.*, vol. 10, no. 1, Jan. 2019, Art. no. 355, doi: 10.1038/s41467-019-08305-y.

[30] A. Martins et al., "On metalenses with arbitrarily wide field of view," *Amer. Chem. Soc. Photon.*, vol. 7, no. 8, pp. 2073–2079, Jun. 2020, doi: 10.1021/acsphotonics.0c00479.

[31] E. Lassalle et al., "Imaging properties of large field-of-view quadratic metalenses and their applications to fingerprint detection," *Amer. Chem. Soc. Photon.*, vol. 8, no. 5, pp. 1457–1468, Apr. 2021, doi: 10.1021/acsphotonics.1c00237.

[32] Y. Guo, X. Ma, M. Pu, X. Li, Z. Zhao, and X. Luo, "High-efficiency and wide-angle beam steering based on catenary optical fields in ultrathin metalens," *Adv. Opt. Mater.*, vol. 6, no. 19, Oct. 2018, Art. no. 1800592, doi: 10.1002/adom.201800592.

[33] E. Tseng et al., "Neural nano-optics for high-quality thin lens imaging," *Nature Commun.*, vol. 12, no. 1, Nov. 2021, Art. no. 6493, doi: 10.1038/s41467-021-26443-0.

[34] A. Arbabi, E. Arbabi, S. M. Kamali, Y. Horie, S. Han, and A. Faraon, "Miniature optical planar camera based on a wide-angle metasurface doublet corrected for monochromatic aberrations," *Nature Commun.*, vol. 7, Nov. 2016, Art. no. 13682, doi: 10.1038/ncomms13682.

[35] B. Groever, W. T. Chen, and F. Capasso, "Meta-lens doublet in the visible region," *Nano Lett.*, vol. 17, no. 8, pp. 4902–4907, Aug. 2017, doi: 10.1021/acs.nanolett.7b01888.

[36] M. Y. Shalaginov et al., "Single-element diffraction-limited fisheye metalens," *Nano Lett.*, vol. 20, no. 10, pp. 7429–7437, Oct. 2020, doi: 10.1021/acs.nanolett.0c02783.

[37] C. Kim, S. J. Kim, and B. Lee, "Doublet metalens design for high numerical aperture and simultaneous correction of chromatic and monochromatic aberrations," *Opt. Exp.*, vol. 28, no. 12, pp. 18059–18076, Jun. 2020, doi: 10.1364/OE.387794.

[38] D. Tang, L. Chen, J. Liu, and X. Zhang, "Achromatic metasurface doublet with a wide incident angle for light focusing," *Opt. Exp.*, vol. 28, no. 8, pp. 12209–12218, Apr. 2020, doi: 10.1364/OE.392197.

[39] J. W. Goodman, *Introduction to Fourier Optics*, 3rd ed. Englewood, CO, USA: Roberts and Publishers, 2005.

[40] P. Chakravarthula, Y. Peng, J. Kollin, H. Fuchs, and F. Heide, "Wirtinger holography for near-eye displays," *Amer. Chem. Soc. Trans. Graph.*, vol. 38, no. 6, pp. 1–13, Nov. 2019, doi: 10.1145/3355089.3356539.

[41] Y. Wang et al., "High-efficiency broadband achromatic metalens for near-IR biological imaging window," *Nature Commun.*, vol. 12, no. 1, Sep. 2021, Art. no. 5560, doi: 10.1038/s41467-021-25797-9.

[42] T. Siefke et al., "Materials pushing the application limits of wire grid polarizers further into the deep ultraviolet spectral range," *Adv. Opt. Mater.*, vol. 4, no. 11, pp. 1780–1786, Jul. 2016, doi: 10.1002/adom.201600250.

[43] H.-H. Hsiao, C. H. Chu, and D. P. Tsai, "Fundamentals and applications of metasurfaces," *Small Methods*, vol. 1, no. 4, Mar. 2017, Art. no. 1600064, doi: 10.1002/smtd.201600064.

[44] C. Kim and B. Lee, "TORCWA: GPU-accelerated Fourier modal method and gradient-based optimization for metasurface design," *Comput. Phys. Commun.*, vol. 282, Jan. 2023, Art. no. 108552, doi: 10.1016/j.cpc.2022.108552.

[45] D. P. Kingma and J. Ba, "Adam: A method for stochastic optimization," in *Proc. Int. Conf. Learn. Represent.*, 2015, pp. 1–41.

[46] M. Hirsch, S. Sra, B. Schölkopf, and S. Harmeling, "Efficient filter flow for space-variant multiframe blind deconvolution," in *Proc. IEEE Comput. Soc. Conf. Comput. Vis. Pattern Recognit.*, 2010, pp. 607–614.

[47] M. Born and E. Wolf, *Principles of Optics: Electromagnetic Theory of Propagation, Interference and Diffraction of Light*, 7th ed. Cambridge, U.K.: Cambridge Univ. Press, 1999.

[48] V. N. Mahajan, "Strehl ratio for primary aberrations in terms of their aberration variance," *J. Opt. Soc. Amer.*, vol. 73, no. 6, pp. 860–861, Jun. 1983.

[49] J. A. Fan, "Freeform metasurface design based on topology optimization," *J. Mater. Res. Bull.*, vol. 45, no. 3, pp. 196–201, Mar. 2020, doi: 10.1557/mrs.2020.62.

[50] K. Miyamoto, "Fish eye lens," *J. Opt. Soc. Amer.*, vol. 54, no. 8, pp. 1060–1061, 1964.

[51] S. W. D. Lim, M. L. Meretska, and F. Capasso, "A high aspect ratio inverse-designed holey metalens," *Nano Lett.*, vol. 21, no. 20, pp. 8642–8649, Oct. 2021, doi: 10.1021/acs.nanolett.1c02612.

[52] Q. Li, M. G. Ji, and J. Kim, "Grayscale nanopixel printing at sub-10-nanometer vertical resolution via light-controlled nanocapillarity," *Amer. Chem. Soc. Nano*, vol. 14, no. 5, pp. 6058–6066, May 2020, doi: 10.1021/acsnano.0c01791.